Dalton Transactions

ROYAL SOCIETY OF CHEMISTRY

PAPER

View Article Online
View Journal | View Issue

Cite this: *Dalton Trans.*, 2022, **51**, 18045

On the performance of a hierarchically porous Ag_2S–Cu_xS electrode in Li-ion batteries†

R. I. Tomov, *[a] L. Mihaylov,[b] L. R. Bird,[a] Ev. Vassileva,[b] R. V. Kumar,[a] M. Chhowalla [a] and T. Spassov [b]

A new binder- and carbon-free electrode for lithium-ion batteries was prepared using a hierarchically porous Ag-based current collector. The latter was produced by applying the method of selective dissolution of the less noble metals from the $Cu_{60}Ag_{30}Al_{10}$ master alloy tape. The current collector was reaction-coated with an electrochemically active Ag_2S–Cu_xS coating. The metallic structure provided a mechanically stable conductive scaffold on the walls of which the Ag_2S–Cu_xS skin material was directly deposited. The ordered porosity – hierarchical and directional – provided easy penetration of the liquid electrolyte as well as short Li^+ ion diffusion paths. The as-prepared electrodes were tested in a half-cell configuration *vs.* Li/Li^+ at various current rates to study the cycling and rate performances of the electrode. The first cycling capacity of ~1250 mA h g^{-1} was measured at 0.4 A g^{-1} current rate. After a rapid decrease, a stable reversible capacity of ~230 mA h g^{-1} was established at a current rate of 0.4 A g^{-1} (calculated *vs.* the weight of the incorporated sulphur). Excellent charge/discharge cycling and rate properties were observed for over 1000 cycles at higher rates of 1.0 and 2.0 A g^{-1}, in the potential window of 0.15–2.8 V *vs.* Li/Li^+. The observed cycling stability was ascribed to the mechanism of a "displacement" reaction with Li ions. Additional capacity is also available from alloying–dealloying with Ag (and Cu to some extent) and S redox reactions. These results open up a new opportunity for using a Cu–Ag alloy as the precursor for making electrodes for thin Li-ion and Li–S batteries with high cycling stability at relatively high current rates.

Received 2nd September 2022,
Accepted 7th November 2022

DOI: 10.1039/d2dt02880h

rsc.li/dalton

Introduction

Commercial lithium-ion batteries (LiBs) are currently an integral part of the sustainable technological development. They have become essential for a wide range of applications – from electric vehicles and stationary energy storage to portable electronics, cellular phones and "internet of things" networks. Conventionally, commercial lithium-ion batteries utilise a variety of graphite-based anodes and pre-lithiated cathodes (*e.g.* $LiCoO_2$, $LiFePO_4$, and $LiMnPO_4$). Although having a number of advantages, graphite-based anodes and intercalation-type cathodes offer low theoretical specific capacity and limited rate performances and are hindered by known safety issues. Thus, significant efforts have been focused on the development of alternative electrode materials exhibiting higher capacity, safer operation and better performance stability.[1–4] Due to their ability to form reversible Li-rich alloys,[5–9] other metallic and semi-metallic elements such as Si (4200 mA h g^{-1} for $Li_{4.4}Si$), Sn (994 mA h g^{-1} for $Li_{4.4}Sn$) and Ag (670/1240 mA h g^{-1} for $Li_{2.7}Ag/Li_5Ag$) have been intensively studied as electrodes for Li-ion secondary batteries. Offsetting the higher cost of precious metals, silver offers several important advantages – high theoretical capacity, high electronic conductivity, low average voltage (~0.175 V (ref. 10)), easy processing and the ability to form a number of intermetallic phases such as α-$Li_{0.9}Ag$, β-$Li_{1.3}Ag$, γ_3-$Li_{2.7}Ag$ and γ_2-Li_5Ag. Using *in situ* X-ray diffraction, Park *et al.*[11] demonstrated that the lithiation limit of Ag particles extends fully until the formation of the γ_2 phase. However, alloy-based Li anodes suffer from a substantial volume change during the lithiation/delithiation reaction – *e.g.*, 236% for the γ_3-$Li_{2.7}Ag$ phase.[10] This results in a gradual mechanical pulverisation of the electrode material and a loss of internal and external (interfacial) electronic conductivity. Such a degradation also leads to parasitic cyclic SEI formation resulting in high irreversible capacity

[a]*Department of Materials Science & Metallurgy, University of Cambridge, Cambridge CB3 0FS, UK. E-mail: rit21@cam.ac.uk*
[b]*Sofia University "St. Kl. Ohridski", Faculty of Chemistry and Pharmacy, 1164 Sofia, Bulgaria*

† Electronic supplementary information (ESI) available. See DOI: https://doi.org/10.1039/d2dt02880h

loss and low initial coulombic efficiency (CE).[12] In order to alleviate the problems caused by the volumetric expansion, three general strategies were experimented:

(i) use of nano-sized active materials;

(ii) use of various buffering carbon additives; and

(iii) formation of active compounds with group 16 chalcogenides (*e.g.* sulphur).

The utilization of an Ag–S electrode system can alleviate some typical disadvantages of the S_8 active mono-material – *e.g.*, the low electrical conductivity,[13] the low rate capability[14] and the high solubility of the reaction polysulphide products Li_2S_n ($3 \leq n \leq 8$) in electrolytes based on polar organic solvents. In a conventional Li–S battery long chain polysulphides Li_2S_n ($6 \leq n \leq 8$) can move between the cathode and the anode resulting in the so-called "shuttle phenomenon".[15] As a result the insoluble products Li_2S_n (n = 1,2) can be deposited onto the anode surface, effectively leading to a loss of the active material, rapid capacity fading and formation of dendritic Li structures.[16]

Utilising the first two approaches, Park *et al.*[11] demonstrated that the electrochemical reaction of Li with Ag is very sensitive to the particle size of silver and the applied current rate. Their slurry coated nano-Ag/C electrodes exhibited the first discharge and charge capacities of 1158 and 727 mA h g^{-1}, respectively, at a low current rate of 0.1 A g^{-1}. The measured cycle retention rate was very low, varying between 5 and 10% (for less than 80 cycles) depending on the current rate (0.1–0.2 A g^{-1}). The third approach was adopted by Hwa *et al.*,[17] who demonstrated an Ag_2S/C nanocomposite electrode with a specific capacity of ~430 mA h g^{-1} after 100 cycles (potential range of 0.0–2.5 V *vs.* Li/Li^+ and a current rate of 0.1 A g^{-1}). During the first discharge, the Ag_2S phase was found to decompose to Li_2S and Ag alloy. During the first charge step, the electrode de-lithiated quasi-reversibly to Ag_2S with some residual nano-Ag and amorphous S phases. Consequently, the reversible capacity of the nano-Ag/C electrode exhibited a tendency of capacity increase over 100 cycles due to the reduced crystallite size of the active materials.

Various transition-metal sulphides have also attracted interest as potential candidates for LIB electrodes due to their diverse structural type, low cost and high theoretical capacity.[18,19] Reversible lithiation/delithiation reactions in some non-layered transition-metal sulphide electrodes (namely Cu_xS and Ag_2S) were previously shown to be controlled by the "displacement lithiation/delithiation mechanism".

$$Me_xS + 2e^- + 2Li^+ \leftrightarrow Li_2S + xM \ (M = Ag, Cu)$$

The latter is promoted by the fast mobility of silver and copper ions and the structural similarity of Ag_2S and Cu_xS (x = 1–2) phases with the Li_2S product.[20,21] Such fast Li^+ kinetics leads to a low voltage hysteresis, a low volume expansion and an improved cycling stability as well as rate performances.[22] Using a slurry coated Ag_2S/C electrode, Hao *et al.*[21] reported first discharge and charge capacities of 209 and 201 mA h g^{-1}, respectively (potential range 1.5 V–2.5 V *vs.* Li/Li+; at 0.2C rate). A relatively good capacity retention close to 88% was achieved after 300 cycles.

Herein, we investigate the performance of an alternative electrode architecture based on an Ag_2S–Cu_xS lithiophilic 3D framework in a half-cell configuration *vs.* Li/Li^+. The electrode is binder- and carbon-free with a controllable hierarchically porous structure. As demonstrated before, the utilisation of lithiophilic 3D electrodes with large surface area, good tortuosity and mechanical strength could improve the wettability of the electrode scaffold with electrolyte, buffer the reaction-related volume changes and reduce the local current densities thus stabilizing the SEI layer.[23,24]

A hierarchically porous structure was obtained by de-alloying a microcrystalline $Cu_{60}Ag_{30}Al_{10}$ tape, applying the method of selective partial dissolution of the less noble metals.[25] Such a porous conductive current collector offers several advantages – (i) high contact surface area of the active material; (ii) easy electrolyte penetration; (iii) short Li ion diffusion paths promoting the kinetics of the electrochemical redox reaction; and (iv) avoidance of the non-active binder phases.

We reported previously[26] a $LiMnPO_4$-olivine cathode deposited on such a porous current collector. The cell demonstrated a stable cycling performance providing an electrochemical capacity of about 120 mA h g^{-1}. In the longer term, we envisage a feasible conjunction of the $LiMnPO_4$-olivine and Ag_2S–Cu_xS electrodes in a thin film battery design where the utilization of a few micron-thick Ag(Cu)-based hierarchically porous current collector would assure a stable performance and high volumetric and gravimetric specific capacity values.

Experimental

The $Cu_{60}Ag_{30}Al_{10}$ master alloy used for the formation of the electrodes with a 3D porous structure was obtained by melting together pure Ag, Cu and Al (all at 99.99% purity). The alloy was homogenized by subsequent melting and solidification under pure Ar flow. A high cooling rate – the melt spinning method (rapid solidification laminar flow casting)[26] – was used to prepare alloy ribbons with a thickness of approximately 50 μm and a width of 1 cm. The angular velocity of the Cu quenching disc used was 2000 rpm. The as-produced alloy ribbon anodes were de-alloyed electrochemically in a three-electrode cell utilising a PARSTAT 2273 potentiostat/galvanostat. The alloy tape was subjected to a selective dissolution under potentiostatic conditions at 350 mV (*vs.* SHE) in an electrolyte aqueous solution of 0.1 M $HClO_4$ with Pt as a counter electrode.

Low-temperature nitrogen adsorption analysis on a Quantachrome Instruments NOVA 1200e (USA) apparatus was used to determine the structural characteristics of the porous structure. The nitrogen adsorption–desorption isotherms were analyzed to evaluate the specific surface area (S_{BET}) on the basis of the BET equation. The total pore volume (V_t) and average pore diameter (D_{av}) were estimated in accordance with

the Gurvich rule at a relative pressure close to 0.99. All samples were outgassed for 15 h under vacuum at 150 °C before the measurements.

The as-produced de-alloyed porous scaffolds were vacuum infiltrated with sulphur dissolved in toluene (C_7H_8, 99%, Alfa Aesar). Controlled volumes (20–40 μL) of the ink were drop-cast on the porous tapes in several steps. After each step, the electrodes were exposed to a low vacuum in order to ensure deep ink penetration. The as-treated tapes were further annealed at 200 °C under flowing Ar gas for 10 min. The active weight of reacted sulphur was estimated by precision micro-scale measurement at ~0.25–0.3 mg cm^{-2}.

Coin half-cells (CR2032) were assembled in an Ar-filled glove box using Celgard tape as a separator, Li foil as a counter electrode, and 1 M $LiPF_6$ in a mixture of ethylene carbonate (EC) and dimethyl carbonate (DMC) as the electrolyte. In order to prevent large volume changes associated with the alloying reaction of Ag and Li at low potentials and focus on the "displacement reaction" mechanism, the potential test window was restricted in the range of 0.15–2.8 V (*vs.* Li/Li+). Electrochemical characterization was carried out at various current rates using a Bio Logic VNP3B-5 workstation. X-ray powder diffraction (CuK_α radiation source, a step size of 2θ = 0.02°, and a counting rate of 1 s per step) was performed using a Bruker D8 Advance diffractometer in an attempt to elucidate the phase of the active material as well as any compositional changes in the electrode post-mortem (due to long cycling). The electrode's morphology and the elemental distribution were studied by high-resolution SEM and EDX (Nova NanoSEM) using acceleration voltages of 5 and 15 kV, respectively.

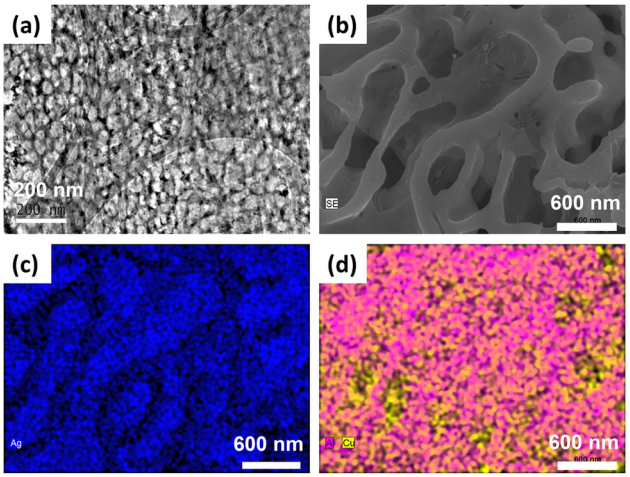

Fig. 1 SEM/EDX images of the (a) master alloy tape and (b) de-alloyed tape; (c) EDX map of Ag; (d) combined EDX map of Cu and Al.

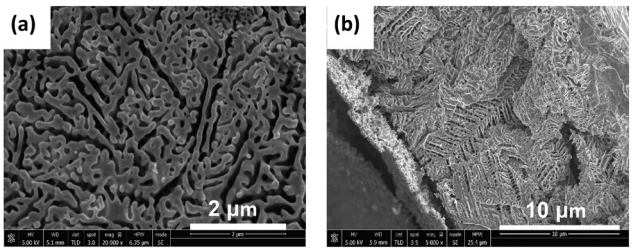

Fig. 2 SEM micrographs of the de-alloyed $Cu_{60}Ag_{30}Al_{10}$ master alloy: (a) top surface and (b) cross-section.

Results and discussion

The elemental analysis of the master alloy tape and the de-alloyed tape showed that after 120 min of potentiostatic treatment the average area tape composition undergoes a change from ~$Cu_{60}Ag_{30}Al_{10}$ to ~$Cu_{10}Ag_{82}Al_{08}$, thus confirming the effect of selective de-alloying and the predominant silver enrichment. Fig. 1(a) and (b) show the comparison of the microstructures of the master alloy tape and the de-alloyed ribbon with a 3D porous architecture, revealing that the latter possesses a well-defined and homogeneous porous architecture uniformly distributed over the whole tape width. As evident from the SEM images shown in Fig. 1(b) and Fig. 2(a) and (b), the ligament sizes range between 100 and 150 nm and the sizes of the macro-pores and the channels vary from 100 nm to 2000 nm. The shifts of Ag (blue), Cu (yellow) and Al (magenta) maps observed in Fig. 1(c) and (d) reflect the original dual phase microstructure – Ag and Cu(Al) solid solutions of the master tape alloy – and the fact that the residual Al is concentrated in the bottom part of the tape, which was effectively not de-alloyed. The higher-magnification (×50 000) cross-sectional image (Fig. 2b) of the de-alloyed part of the tape shows a distinctive "pine tree"-shaped porous scaffold combining larger elongated channels with smaller micro-pores.

The specific surface area S_{BET} = ~2 m^2 g^{-1} of the de-alloyed tape was determined on the basis of the BJH method. The total pore volume (V_t = 0.007 cm^3 g^{-1}) and the average pore diameter (D_{av} = 15 nm) were estimated in accordance with the Gurvich rule at a relative pressure close to 0.99 (see the nitrogen absorption isotherm in Fig. 3a). Fig. 3(b) shows the differential pore volume *versus* diameter plot, demonstrating the dominant contribution of nano-sized pores (ranging from 4 to 12 nm) in the total pore size distribution. The mismatch between the dominant pore size observed by SEM and the one determined by nitrogen adsorption should be noted. This discrepancy could be explained by the presence of a large number of very small pores, which could not be evidenced by the SEM analysis.

A comparison of the XRD patterns collected from the coated electrode against the pristine de-alloyed non-coated substrate is presented in Fig. 3b. It confirms the presence of the expected monoclinic α-Ag_2S phase (space group *P*21/*c* (14)) accompanied by the tetragonal Ag_3CuS_2 (space group *I*41/*amd*) and orthorhombic $(Ag,Cu)_2S$ (space group *Cmc*21) intermetallic phases. The latter analysis corresponds well with the SEM/EDX data collected from an as-coated electrode (see Fig. 4a and b).

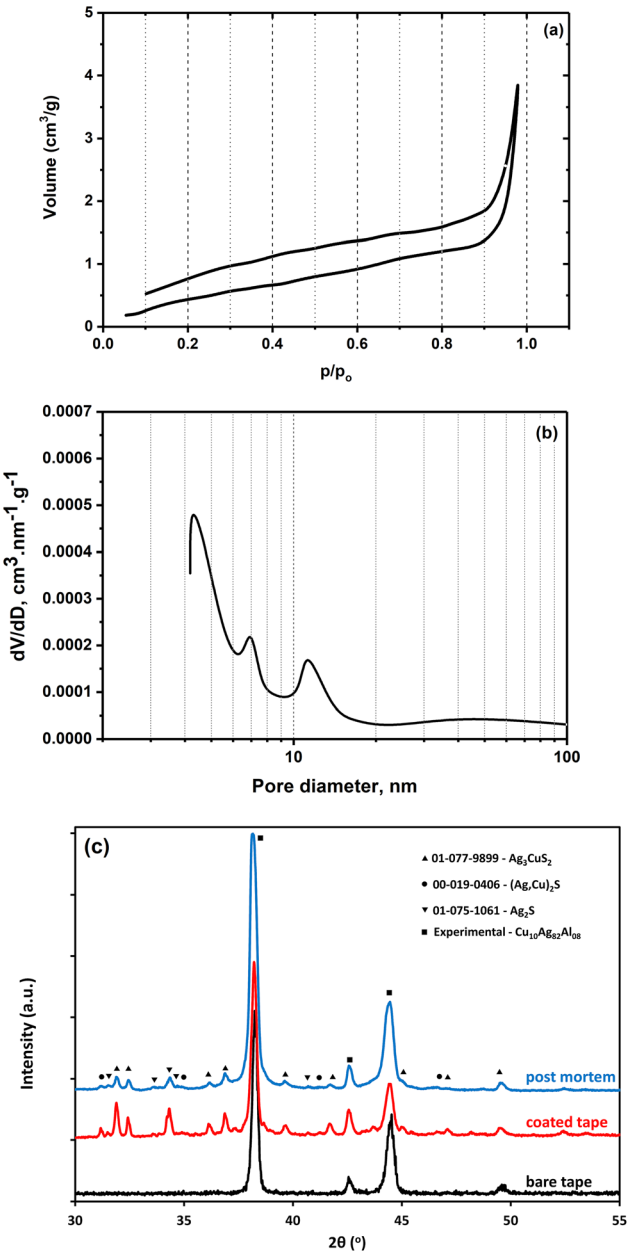

Fig. 3 (a) Nitrogen adsorption–desorption isotherm for de-alloyed tape obtained by the Barrett, Joyner and Halenda method; (b) Differential pore volume *versus* diameter plot; (c) Comparison of the XRD patterns of de-alloyed non-coated substrate and coated electrode.

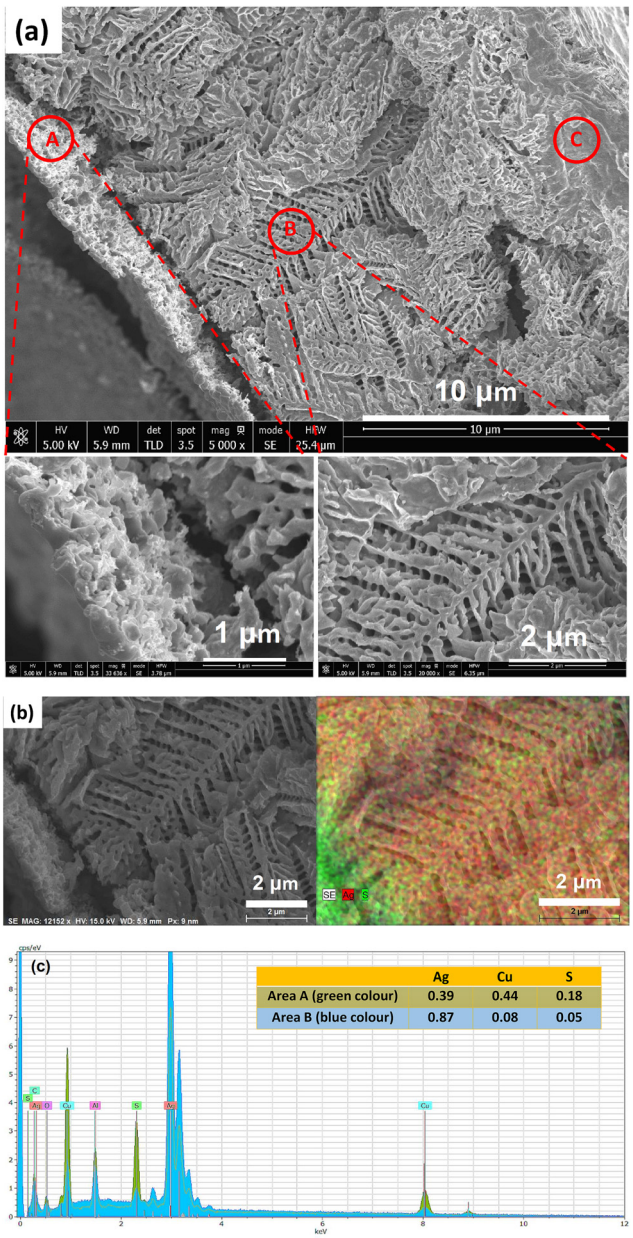

Fig. 4 Cross-sectional SEM images (a) and EDX Ag and S maps (b) of the infiltrated and thermally treated electrodes; (c) EDX spectra of areas (A) and (B) shown in (a) and the relevant average composition ratios.

Three different morphologically distinctive areas are marked with red capital letters. Region A represents a submicron (~250 nm) thick amorphous/nano-crystalline sulphur-rich "skin" layer at the top surface of the tape. For comparison, a cross-sectional HR-SEM image of the bare de-alloyed ribbon is presented in Fig. S1.† It is apparent that no "skin" layer can be seen on the top surface. Thus, one can assume that the sulphur-rich membrane observed in region A in Fig. 4a is comprised of excess elemental sulphur. As no crystalline form of elemental sulphur was detected by XRD (see Fig. 3b) we speculate that the sulphur in the layer is present in its vitreous form resulting from the quenching step after annealing in Ar gas. Region B clearly delineates the de-alloyed part of the tape with an average composition of $Cu_{10}Ag_{82}Al_{08}$ infiltrated with sulphur. Region C corresponds to the original dense bottom part of the $Cu_{60}Ag_{30}Al_{10}$ master alloy. The accumulation of sulphur forming a porous top membrane layer A is illustrated by the elemental mapping of a cross-section area in Fig. 4b and a summary of the EDX results in Fig. 4c. The lack of S_8 crystalline peaks is observed in Fig. 3(b). The distribution of sulphur within the porous "pine-tree" structure appears to be

uniform, without any large segregations, suggesting the good wetting of the substrate skeleton by a toluene-based ink.

The initial electrochemical charge/discharge test at a low current rate of 0.1 A g^{-1} (calculated *vs.* the weight of incorporated sulphur) promoted near equilibrium conditions, localising the electrochemical reaction to the region of the electrode/electrolyte interface. The discharge process was very slow plateauing at ~1.8–1.9 V due to the kinetic barrier presented by the sulphur-rich membrane. A specific discharge capacity limit was set at 600 mA h g^{-1} in order to introduce a practical experimental time frame. Fig. 5(a) shows that while the specific charge capacity was observed to increase steadily with each consecutive cycle the end potential decreased from 1.95 V (for cycle 1) to 1.7 V (for cycle 10). Considering the observed dynamics of the specific charge capacities, the end-potentials and the chemical composition of the "skin" membrane (see Fig. 4c), we speculate that at 0.1 A g^{-1} current rate this behaviour accounts for the confinement of the reaction in the elemental sulphur-rich (S_8) coating. Thus, the sulphur in the "skin" layer gradually solvates due to the formation of long chain polysulphides Li_2S_n ($6 \leq n \leq 8$) at a potential of ~1.9 V.[27,28]

In the initial several cycles, two reduction plateaus are observed:[29]

(i) First, an oblique plateau at ~2.1–2.2 V where polysulphides with $n \sim 6$–8 are generated with the acceptance of 0.5 electron per atom of sulfur.

$$S_8^{0} + 4e^- = 2S_4^{2-}$$

(ii) Second, an apparent plateau for $n < 4$ at ~1.9–2.0 V reflecting the acceptance of an additional electron per sulfur atom.

$$S_4^{2-} + 4e^- = 2S^{2-} + S_2^{2-}$$

The low capacity of the first charge suggests that it does not lead to the transformation of polysulphides into elemental sulfur thus illustrating slow dissolution of the "skin" layer. The capacity evolution of the following charges reflects the establishment of the shuttle mechanism where lower-order polysulphides formed at the lithium electrode diffuse back to generate the higher forms of polysulphides.

The additional sloping plateau appearing at cycle 10 accounts for the Li storage in the Ag_2S–Cu_xS electrode driven by the displacement lithiation/delithiation reaction.

A summary of the charge/discharge test at a higher rate of 0.4 A g^{-1} is presented in Fig. 5(b). In the potential window of 2.8–0.15 V the first discharge specific capacity exceeded 1200 mA h g^{-1}, suggesting partial removal of the membrane kinetic barrier. It is noted that the low initial coulombic efficiency of ~75% was due to the formation of an SEI layer. The solvation of the residual unreacted sulphur led to a rapid decrease in the specific capacity over the first two cycles. Further cycling resulted in multi plateau shaped charge/discharge cycle curves within the potential window of 2.8–0.15 V and a gradual decrease in the specific capacity reaching a

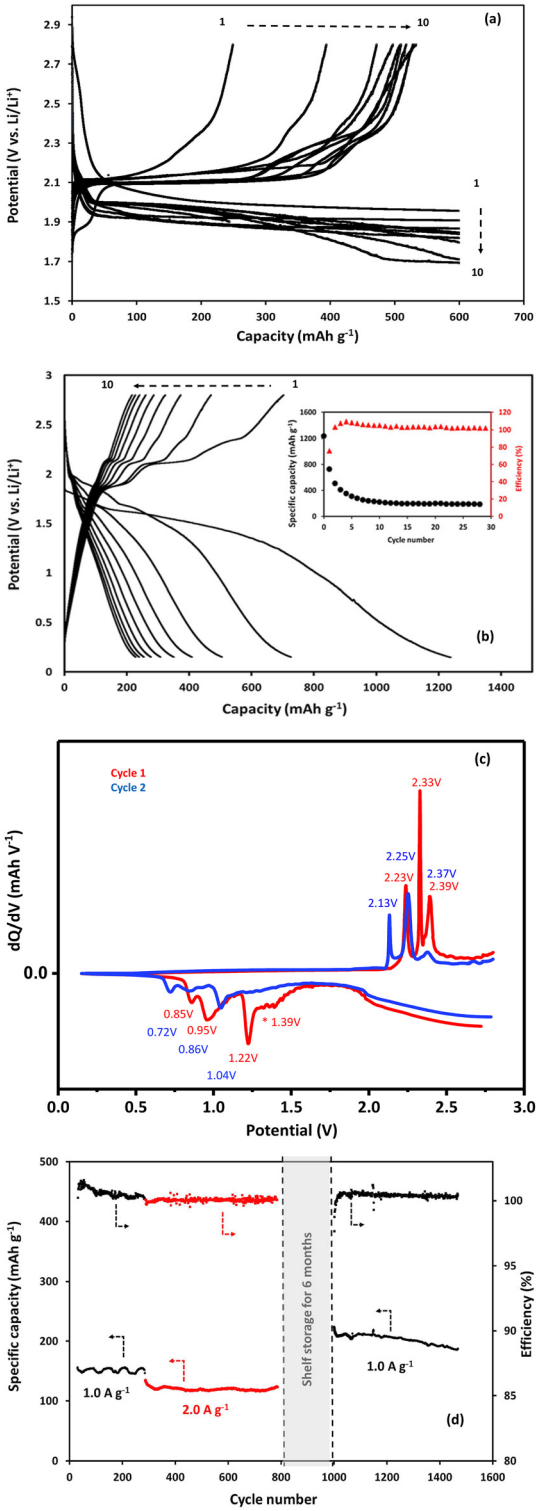

Fig. 5 (a) Potential *vs.* capacity plots for the first 10 cycles of the Ag_2S–Cu_xS electrode at 0.1 A g^{-1} current rate; (b) potential *vs.* capacity plots for the first 10 cycles of the Ag_2S–Cu_xS electrode at 0.4 A g^{-1} current rate (the inset shows the evolution of the capacity and efficiency for the first 30 cycles); (c) differential capacity plot of the Ag_2S–Cu_xS electrode for the first two cycles at 0.4 A g^{-1} current rate; and (d) long-term cycling performances at the current rates of 1 A g^{-1} and 2 A g^{-1}.

stable value of 230 mA h g^{-1} after ~15 cycles (see the inset in Fig. 5b). The latter value corresponds well with the one previously reported for an Ag_2S electrode by Hao *et al.*[21] (215 mA h g^{-1}). This behaviour suggested that the initial rapid capacity decrease was due to the irreversible formation of an SEI layer and the solvation of polysulfides followed by stable cycling associated with the Ag_2S–Cu_xS displacement reaction.

Three-dimensional current collectors of the reported thickness (approximately 50 μm) are expected to possess low volumetric energy density. In order to estimate the effect of the Ag_2S–Cu_xS active coating on the volumetric densities the energy density of the Ag_2S–Cu_xS electrode at 0.4 A g^{-1} current rate was normalized to the electrode surface area and compared with the one measured for a bare Ag electrode – see Fig. S2(a) and (b).† The latter was tested in an identical half-cell configuration. The comparison revealed that coating the 3D skeleton of the bare silver electrode with a submicron thick Ag_2S–Cu_xS layer led to more than one order of magnitude increase in the volumetric density. Moreover, while the capacity of the Ag_2S–Cu_xS electrode reached a stable value at cycle number 10, the capacity of the bare Ag electrode, after an initial decrease for the first 5 cycles, showed an increasing trend (see the insets of Fig. S2†), demonstrating the continuous pulverization effect of Ag in the lithiation/delithiation process.

In comparison, the nanocomposite Ag_2S/C electrodes reported by Hwa *et al.*[17] tested in a wider voltage range of 0.0–2.5 V exhibited a higher capacity of 430 mA h g^{-1} after 100 cycles accumulated by a combination of "displacement" and "alloying/de-alloying" reactions as shown in Fig. 6:

The measured capacity of 230 mA h g^{-1} slightly exceeds the theoretical capacity for Ag_2S (217 mA h g^{-1}), which suggests that in the present work, one has to account for the capacity contribution of the Cu_xS component. Although representing less than 10% of the overall electrode composition, the Cu_xS component contributes a higher specific theoretical capacity of ~560 mA h g^{-1} (for $x = 1$). Débart *et al.*[20] analysed in detail the charge/discharge reaction mechanism related to the Cu_xS electrode. They concluded that the reacting path includes an initial formation of a polymorphic $Cu_{2-x}S$ intermediary phase, which transformed further to Cu + Li_2S as shown in Fig. 6(b).

The non-normalized differential capacity plot (DCP) in Fig. 5(c) supports this assumption by revealing several peaks associated with a multistep reversible reaction mechanism of the $(Ag_x,Cu_y)S_z$ intermetallic phases with Li^+ in the potential window from 1.3 V to 0.7 V (discharging) and 2.4 to 2.0 V (charging). During the first cycle, three reduction peaks located at 1.22, 0.95 and 0.85 V are resolved indicating the multistep reduction process described in Fig. 6(a) and (b). The oxidation peaks observed at around 2.39, 2.33 and 2.23 V are ascribed to the corresponding de-lithiation reactions. In the second cycle, the position of the peaks shifts to the left. Such a migration can be attributed to the overpotential caused by the resistance change resulting from the dissolution of the sulphur-rich "skin" membrane. The potential area above 2.0 V is covered by a broad hump obscuring the peaks commonly associated with the conversion of sulfur to high-order polysulphides.[30] The broad peak that resolved at ~1.4 V and disappeared in cycle 2 could be assigned to the formation of an SEI in the first cycle.

The Ag_2S–Cu_xS electrode was subjected to long-term cycling and the data summary is shown in Fig. 5(d). After testing at 1 A g^{-1} and 2 A g^{-1} current rates the cell was rested for 6 months and re-tested at 1 A g^{-1} current rate. Stable cycling performances of the Ag_2S–Cu_xS electrode were recorded for over 1200 cycles:

I. 250 cycles at 1 A g^{-1} current rate – an average specific capacity of ~150 mA h g^{-1} with a retention of ~98%;

II. 500 cycles at 2 A g^{-1} current rate – an average specific capacity of 120 mA h g^{-1} with a retention of ~97%;

III. 450 cycles at 1 A g^{-1} current rate – an average specific capacity of ~200 mA h g^{-1} with a retention of ~85%.

The observed stable cycling behaviour and rate performances could be attributed to the nature of the "displacement" reaction, which is promoted by the high mobility of silver, copper and lithium ions in the metal sulphide electrode. The diffusion coefficients of Ag^+ and Li^+ ions in the Ag_2S phase measured and calculated by different authors are summarised in Table 1. The data clearly suggest approximately one order of magnitude difference in the diffusion coefficients of Ag^+ and Li^+ ions in the Ag_2S matrix. Consequently, during the reduction phase Ag and Cu diffuse to the surface and form randomly directed dendrites encompassing the Li_2S matrix.[20]

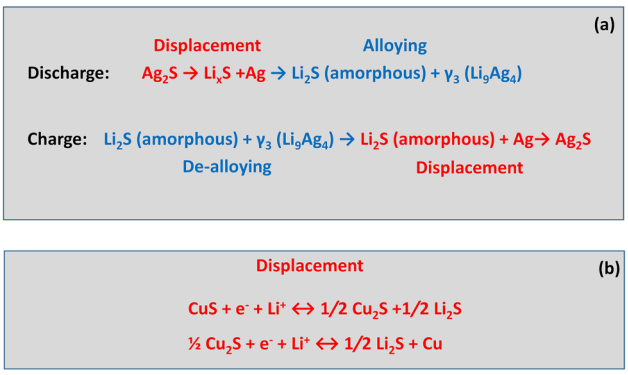

Fig. 6 Combination of reactions involved in charge/discharge cycles of the Ag_2S electrode in the 2.8–0 V potential window.

Table 1 Summary of published data on the diffusion coefficients and activation energies of Ag and Li in an Ag_2S matrix

Ion	Lattice	Diffusion coefficient (cm^2 s^{-1})	Activation energy (eV)	Method
Ag^+	Ag_2S	7.34×10^{-10}	0.4	Calculated[37]
	Ag_2S	1.97×10^{-7}	—	Experimental[38]
Li^+	Ag_2S	2.34×10^{-11}	0.52	Calculated[32]
	Ag_2S	$\sim 10^{-8}$	—	Experimental[21]

Reversibly, during the charge stage, Li is extracted and (Ag, Cu) sulphide compounds are re-oxidised to metal sulphides. We speculate that the stable charge/discharge cycling at higher rates of 1 A g^{-1} and 2 A g^{-1} observed in this work is a result of the described process, which largely avoids the pulverisation corrosion and suppresses the dissolution of polysulphide intermediates (Li_2S_n) ($4 \leq n \leq 8$) by physical immobilization. Several groups have previously reported Cu_xS electrodes with enhanced capacity retention at high rates when an excess of copper is present to immobilize the active sulphur elements.[31–33]

After a period of shelf storage (~6 months), the re-tested electrode exhibited a noticeable jump in the specific capacity (see Fig. 5(d)). This phenomenon could be explained by the fact that some slow erosion of the electrode wall at higher current rates nevertheless took place resulting in an extension of the active surface area by the formation of a nanostructured top layer. During the long shelf storage, this part of the electrode wall would react with the dissolved polysulphides forming a new portion of the active metal sulphide coating. In support of this hypothesis is the previously published experimental and modelling study by Xi *et al.*[34] reporting on the evidence of a strong catalytic effect of transition metal sulphides on the cleavage reaction of high-order polysulphides. One can speculate that the Ag and Cu nanoparticles present on the ligament surface can be oxidized by the polysulphides to form Ag_2S and Cu_xS_y. The as-created enhanced active surface area would contribute to the observed increase in the specific capacity.

Post-mortem SEM/EDX analyses were performed after the completion of the cycling tests. The high-resolution top surface image and cross-sectional elemental maps of the Ag_2S–Cu_xS electrode are presented in Fig. 7. It is apparent that after more than 1000 cycles, the electrode preserved its porous architecture and mechanical integrity. A ligament wall thickness of ~80–100 nm was detected, confirming the absence of substantial pulverization during the electrode operation (see Fig. 7a). The EDX mapping also confirms the uniform distribution of sulphur in the Ag matrix (see Fig. 7b).

The long-term cycling results suggest an important application of the Ag_2S–Cu_xS nanocomposite as a polysulfide dissolution inhibitor *via* strong interactions with the polysulfides during the redox processes. It effectively adsorbs the polysulfides thus reducing the shuttling effect and improving the long-time battery performance. A number of such adsorbing additives (*e.g.*, Ti_4O_7 and MnO_2 nanosheets) have been proposed by Nazar *et al.*[35,36] with promising efficiency. In contrast to those metal oxide additives, the Ag_2S–Cu_xS nanocomposite contributes additional capacity in the voltage range above 1.5 V. Additionally, the proposed electrode produces a conductive metal in the reversible reaction thus improving the electronic conductivity of the electrode.

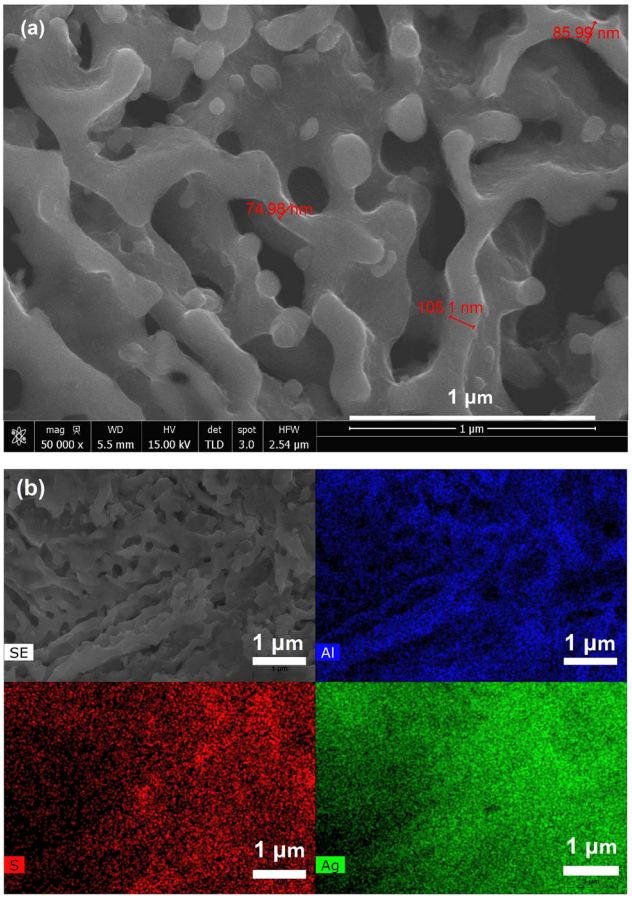

Fig. 7 Post-mortem SEM/EDX analyses: (a) top view of the Ag(Cu)S electrode and (b) cross-sectional EDX mapping of Ag, S and Al distribution.

Conclusions

Hierarchically porous 3D Ag_2S–Cu_xS current collectors were prepared by simple electrochemical de-alloying. The electrodes were electrochemically tested in a half-cell configuration *vs.* Li/Li^+. A reversible specific capacity of ~230 mA h g^{-1} was measured at a current rate of 0.4 µA cm^{-2}. The electrode performance was shown to be stable over 1000 cycles at 1 and 2 A g^{-1} current rates. This longevity and rate performance were attributed to the displacement reaction of the Ag_2S–Cu_xS active material with Li ions.

Future research will focus on the fabrication of hierarchically porous current collectors based on the deposition of Ag alloy coatings on thin polymer substrates with subsequent selective de-alloying.

Considering the relative technological simplicity of the procedure, the proposed electrode architecture could be a commercially viable alternative for the development of high-performance solid-state batteries and "anode-free" batteries, which have attracted substantial interest recently. The latter battery concept avoids the use of excess Li by coupling lithiophilic current collectors with lithium-rich materials as cathodes, such as Li_2S, $LiFePO_4$, *etc*. During the initial charge, lithium can be uniformly deposited onto the surface of the 3D

porous collector, which provides a high density of nucleation sites thus reducing the local current density and suppressing the Li dendrite formation.

Author contributions

R.I. Tomov: conceptualization, methodology, experimentation, validation, investigation, writing – review and editing; L. Mihaylov: experimentation, characterization, validation, review and editing; L. R. Bird: experimentation, characterization, validation, review and editing; Ev. Vassileva: experimentation, characterization, review and editing; R. V. Kumar: conceptualization, methodology, writing – review and editing; M. Chhowalla: conceptualization, supervision, project administration, review and editing; and T. Spassov: conceptualization, supervision, project administration, review and editing.

Conflicts of interest

There are no conflicts to declare.

Acknowledgements

This work was supported by the European Regional Development Fund within the Operational Programme "Science and Education for Smart Growth 2014–2020" under the Project CoE "National Center of Mechatronics and Clean Technologies" "BG05M2OP001-1.001-0008" and the EPSRC – OperMAD project EP/T001038/1 "Expanding the Environmental Frontiers of Operando Metrology for Advanced Device Materials Development".

References

1 J.-M. Tarascon and M. Armand, Issues and Challenges Facing Rechargeable Lithium Batteries, *Nature*, 2001, **414**, 359–367.
2 A. S. Arico, P. Bruce, B. Scrosati, J.-M. Tarascon and W. van Schalkwijk, Nanostructured Materials for Advanced Energy Conversion and Storage Devices, *Nat. Mater.*, 2005, **4**, 366–377.
3 M. Armand and J.-M. Tarascon, Building Better Batteries, *Nature*, 2008, **451**, 652–657.
4 J. B. Goodenough and Y. Kim, Challenges for Rechargeable Li Batteries, *Chem. Mater.*, 2010, **22**, 587–603.
5 A. N. Dey, Electrochemical Alloying of Lithium in Organic Electrolytes, *J. Electrochem. Soc.*, 1971, **118**, 1547–1549.
6 H. Wu and Y. Cui, Designing nanostructured Si anodes for high energy lithium ion batteries, *Nano Today*, 2012, **7**, 414–429.
7 C.-M. Park, J.-H. Kim, H. Kim and H.-J. Sohn, Li-alloy based anode materials for Li secondary batteries, *Chem. Soc. Rev.*, 2010, **39**, 3115–3141.
8 M. S. Wittingham, Inorganic nanomaterials for batteries, *Dalton Trans.*, 2008, 5424.
9 P. G. Bruce, B. Scrosati and J.-M. Tarascon, Nanomaterials for Rechargeable Lithium Batteries, *Angew. Chem., Int. Ed.*, 2008, **47**, 2930–2946.
10 M. N. Obrovac and V. L. Chevrier, Alloy Negative Electrodes for Li-Ion Batteries, *Chem. Rev.*, 2014, **114**, 11444–11502.
11 C.-M. Park, H. Jung and H.-J. Sohn, Electrochemical Behaviors and Reaction Mechanism of Nanosilver with Lithium, *Electrochem. Solid-State Lett.*, 2009, **12**(9), A171–A175.
12 J. Lu, Z. Chen, F. Pan, Y. Cui and K. Amine, High-Performance Anode Materials for Rechargeable Lithium-Ion Batteries, *Electrochem. Energy Rev.*, 2018, **1**, 35–53.
13 *Lange's Handbook of Chemistry 3rd edn*, ed. J. A. Dean, McGraw-Hill, 1985, pp. 3–5.
14 R. D. Rauh, F. S. Shuker, J. M. Marston and S. B. Brummer, Formation of lithium polysulfides in aprotic media, *Inorg. Nucl. Chem.*, 1977, **39**, 1761–1766.
15 Y. V. Mikhaylik and J. R. Akridge, Polysulfide Shuttle Study in the Li/S Battery System, *J. Electrochem. Soc.*, 2004, **151**(11), A1969–A1976.
16 Z. Li, J. Huang, B. Y. Liaw, V. Metzler and J. B. Zhang, A review of lithium deposition in lithium-ion and lithium metal secondary batteries, *J. Power Sources*, 2014, **254**, 168–182.
17 Y. Hwa, C.-M. Park and H.-J. Sohn, The electrochemical characteristics of Ag_2S and its nanocomposite anodes for Li-ion batteries, *J. Electroanal. Chem.*, 2012, **667**, 24–29.
18 Y. Lu, B. Li, S. S. Zheng, Y. X. Xu, H. G. Xue and H. Pang, Syntheses and energy storage applications of M_xS_y (M=Cu, Ag, Au) and their composites: rechargeable batteries and supercapacitors, *Adv. Funct. Mater.*, 2017, **27**, 1703949.
19 P. B. Geng, S. S. Zheng, H. Tang, R. M. Zhu, L. Zhang, S. Cao, H. G. Xue and H. Pang, Transition metal sulfides based on graphene for electrochemical energy storage, *Adv. Energy Mater.*, 2018, **8**, 26.
20 A. Débart, L. Dupont, R. Patrice and J.-M. Tarascon, Reactivity of transition metal (Co, Ni, Cu) sulphides versus lithium: The intriguing case of the copper sulphide, *Solid State Sci.*, 2006, **8**, 640–651.
21 W. Hao, H. Si, X. Cheng, W. Zhu and X. Qiu, Displacement reaction-based Ag_2S electrode for lithium batteries with high volumetric energy density, *Solid State Ionics*, 2019, **340**, 115015.
22 M. T. McDowell, Z. D. Lu, K. J. Koski, J. H. Yu, G. Y. Zheng and Y. Cui, In situ observation of divergent phase transformations in individual sulfide nanocrystals, *Nano Lett.*, 2015, **15**, 1264–1271.
23 K. Ye, Y. Xia and Z. Li, $A_{g2}S$-modified 3D Carbon Cloth as a Dendrite Suppressing Framework for High Energy Lithium-Sulfur Batteries, *Chem. Lett.*, 2022, **51**, 504–507.
24 D. Xie, Y.-P. Zheng, M. Zahid, Y.-F. Li, W.-Y. Diao, F.-Y. Tao, Z.-F. Yang, H.-Z. Sun, X.-L. Wu and J.-P. Zhang, *J. Colloid Interface Sci.*, 2022, **609**, 606–616.

25 J. Erlebacher, M. J. Aziz, A. Karma and K. Sieradzki, Evolution of nanoporosity in dealloying, *Nature*, 2001, **410**, 450–453.
26 L. Mihaylov, T. Boyadzhieva, R. Tomov, C. V. Kumar, V. Koleva, R. Stoyanova and T. Spassov, $LiMnPO_4$-olivine deposited on a nanoporous alloy as an additive-free electrode for lithium ion batteries, *Dalton Trans.*, 2019, **48**, 17037–17044.
27 C.-M. Park, Y. Hwa, N.-E. Sung and H.-J. Sohn, Stibnite (Sb2S3) and its amorphous composite as dual electrodes for rechargeable lithium batteries, *J. Mater. Chem.*, 2010, **20**, 1097–1102.
28 H. Yamin, A. Gorenshtein, J. Penciner, Y. Sternberg and E. Peled, Lithium Sulfur Battery -Oxidation/Reduction Mechanisms of Polysulfides in THF Solutions, *J. Electrochem. Soc.*, 1988, **135**, 1045–1048.
29 Y. V. Mikhaylik and J. R. Akridge, Polysulfide Shuttle Study in the Li/S Battery System, *J. Electrochem. Soc.*, 2004, **151**(11), A1969–A1976.
30 G. Zhou, H. Tian, Y. Jin, X. Tao, B. Liu, R. Zhang, Z. Wei Seh, D. Zhuo, Y. Liu, J. Sun, J. Zhao, C. Zu, D. Sichen Wu, Q. Zhang and Y. Cui, Catalytic oxidation of Li2S on the surface of metal sulfides for Li–S batteries, *Proc. Natl. Acad. Sci. U. S. A.*, 2017, **114**(5), 840–845.
31 Z. Zhang, Y. An, J. Feng, L. Ci, B. Duan, W. Huang, C. Dong and S. Xiong, Carbon coated copper sulfides nano sheets synthesized via directly sulfurizing Metal-Organic Frameworks for lithium batteries, *Mater. Lett.*, 2016, **181**, 340–344.
32 H. Li, Y. Wang, J. Huang, Y. Zhang and J. Zhao, Microwave-assisted Synthesis of CuS/Graphene Composite for Enhanced Lithium Storage Properties, *Electrochim. Acta*, 2017, **225**, 443–451.
33 C. Ding, D. Su, W. Ma, Y. Zhao, D. Yan, J. Li and H. Jin, Design of hierarchical CuS/graphene architectures with enhanced lithium storage capability, *Appl. Surf. Sci.*, 2017, **403**, 1–8.
34 K. Xi, D. He, C. Harris, Y. Wang, C. Lai, H. Li, P. R. Coxon, S. Ding, C. Wang and R. V. Kumar, Enhanced Sulfur Transformation by Multifunctional FeS_2/FeS/S Composites for High-Volumetric Capacity Cathodes in Lithium–Sulfur Batteries, *Adv. Sci.*, 2019, **6**(6), 1800815.
35 Q. Pang, D. Kundu, M. Cuisinier and L. F. Nazar, Surface-enhanced redox chemistry of polysulphides on a metallic and polar host for lithium-sulphur batteries, *Nat. Commun.*, 2014, **5**, 4759.
36 X. Liang, C. Hart, Q. Pang, A. Garsuch, T. Weiss and L. F. Nazar, A highly efficient polysulfide mediator for lithium–sulfur batteries, *Nat. Commun.*, 2015, **6**, 5682.
37 R. R. Oliveira, B. N. C. Tenorio and A. B. Rocha, Ab initio study of diffusion of hydrogen, silver and lithium in PbS and Ag_2S, *Comput. Mater. Sci.*, 2019, **166**, 75–81.
38 R. L. Allen and W. J. Moore, Diffusion of silver in silver sulfide, *J. Phys. Chem.*, 1959, **63**, 223–226.